Magnetic Induction Micromachine—Part II: Fabrication and Testing

Florent Cros, Hur Koser, *Member, IEEE*, Mark G. Allen, *Senior Member, IEEE*, and Jeffrey H. Lang, *Fellow, IEEE*

***Abstract*—This paper presents the realization of a magnetic induction machine. The development of this machine is part of an ongoing project to create high-power density electric microgenerators for use in portable-power applications. The results reported here focus on testing a first-generation nonlaminated electromagnetic actuator, a metrology device designed for exploring and characterizing the fabrication process and the operating behavior of the magnetic induction micromachine. Achieving high power density requires large electrical currents and magnetic fluxes, which necessitate thick, multilayered microstructures that are difficult to fabricate. The batch-fabrication schemes developed as part of this work are based on low-temperature micromolding that makes extensive use of various ultra-thick photoresists and electroplating of electrical conductors (Cu) and ferromagnetic materials (Ni-Fe 80%-20%), resulting in the successful fabrication of a multilayer two-phase planar stator and a planar rotor. To evaluate the performance of the complete machine (stator plus rotor), a 4-mm-diameter, 500-μm-thick electroplated Ni-Fe rotor is tethered to a series of flexible structures that prevent it from making a complete revolution, but allow accurate torque performance extraction. The tethered induction micromotor studied here exhibits torque production as high as 4.8 μN·m. [1436]**

***Index Terms*—Magnetic induction micromachine, micromolding, electroplating, tethers, micromotor.**

I. Introduction

RECENTLY there has been much interest in Power MEMS, i.e., the generation of mechanical and electrical power on the small scale for use in military and commercial applications. Examples of such programs include various gas-turbine efforts [1], [2]. In this work, we seek to develop a generator that can take as input mechanical work generated from a power MEMS platform and convert that mechanical work to electrical energy. The eventual power levels anticipated from such machines are in the range of tens of watts. In order to achieve these power levels, large rotational speeds, on the order of hundreds of thousands of revolutions per minute or higher, are contemplated.

Manuscript received September 28, 2004; revised June 19, 2005. This work was supported by the Army Research Office under Research Grant DAAG55-98-1-0292 and by DARPA under Research Grant DABT63-98-C-0004. Subject Editor J. Judy.

F. Cros was with the School of Electrical and Computer Engineering, Georgia Institute of Technology, Atlanta, GA 30332 USA. He is now with the Cardiomems Inc., Atlanta, GA 30308 USA (e-mail: fcros@cardiomems.com).

H. Koser is with the Electrical Engineering Department, Yale University, New Haven, CT 06520 USA (e-mail: hur.koser@yale.edu).

M. G. Allen is with the School of Electrical and Computer Engineering, Georgia Institute of Technology, Atlanta, GA 30332 USA.

J. H. Lang is with the Electrical Engineering and Computer Science Department, and the Laboratory for Electrical and Electronic Systems, Massachusetts Institute of Technology, Cambridge, MA 02139 USA (e-mail: lang@mit.edu).

Digital Object Identifier 10.1109/JMEMS.2006.872239

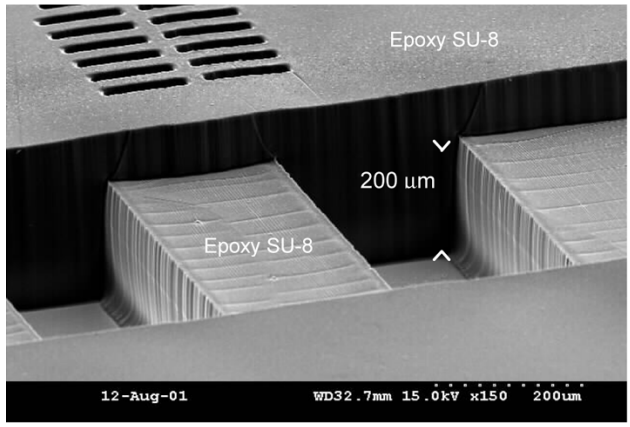

Fig. 1. SEM photograph of a 200-μm-tall SU-8 mold, spun and successfully patterned on top of preexisting high-aspect ratio structures.

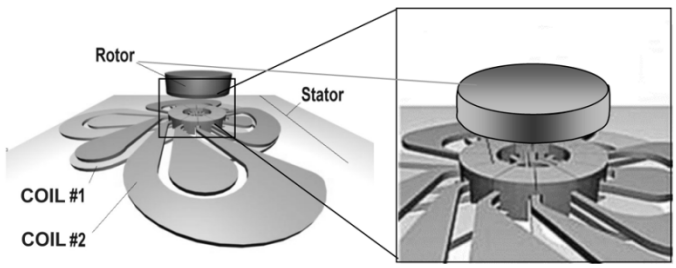

Fig. 2. The topology of a complete machine. The rotor is suspended over the stator via air bearings. The tethers are not shown.

Induction machines are interesting candidates for power-MEMS electromechanical energy conversion, since no electrical connection to the rotor is required (which would be difficult to achieve at such high rotational speeds). Induction machines based on either electrostatic [3] or magnetic [4] approaches can be contemplated. This paper will focus on magnetic induction machines for several reasons. First, as the torque and power targets for electromechanical energy conversion increase, so too will the size of the machines that perform the conversion. This increase is already sufficient for magnetic machines to be favored generally over electric machines in terms of torque and power density. One direct observation is that magnetic induction machines can operate with rotor-stator gaps much larger than is practical for electric induction machines [3], [4]. This results in greatly reduced windage (i.e., fluid-mechanical drag) losses, thereby increasing overall system efficiency. Moreover, magnetic machines are

1057-7157/$20.00 © 2006 IEEE

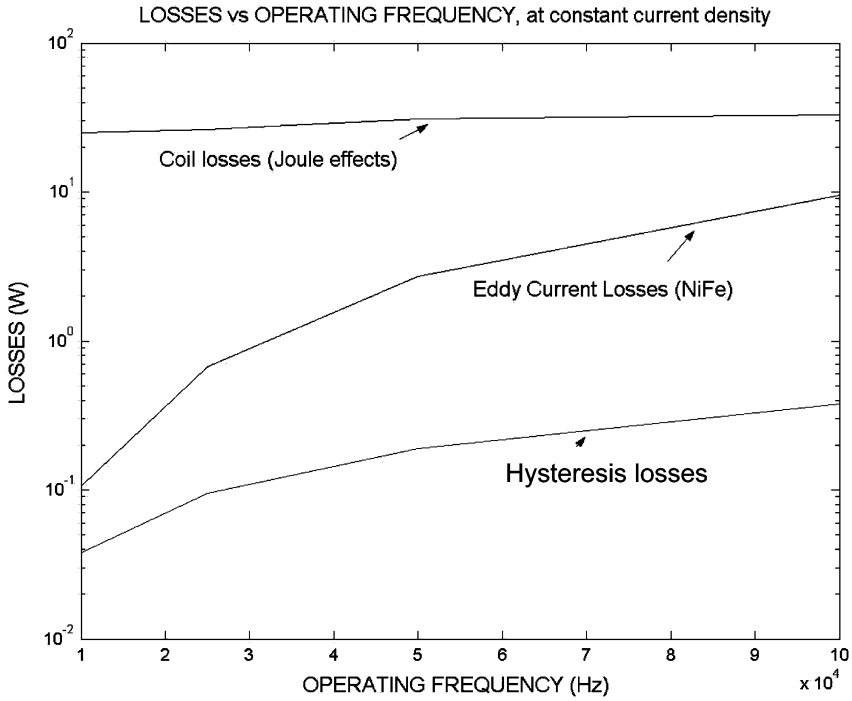

Fig. 3. Losses in the stator as a function of operating frequency. Both Joule effects and eddy-current losses are calculated using a 2-D magnetic quasistatic ANSYS analysis. Hysteresis losses are calculated from material data. The dependence of coil losses on frequency is due to the skin effect.

inherently low-voltage, high-current, and low-frequency machines. They are therefore better matched to their end-use in the portable power applications of interest (e.g., portable power-systems for miniature communication components and wearable electronics), and their associated power electronics can be much more compact and efficient.

In this article, we present a detailed description of the fabrication and testing of both the stator and the tethered rotor of a magnetic induction micromachine. This first-generation machine does not address the additional fabrication difficulty associated with creating suitably laminated ferromagnetic cores for micron-scale, low-megahertz-range applications which is the subject of concurrent research efforts [5]–[7]. In this work, fabrication complexity is also mitigated through the use of materials with either low Curie or low-decomposition temperatures, which limits the operating temperatures to lower than 400 °C, which may be sufficient for low-temperature power-MEMS applications.

II. Fabrication-Constrained Device Design

A typical macroscale induction machine consists of a high-aspect ratio cylindrical "squirrel-cage" rotor and three-dimensionally wrapped stator coils and magnetic pole pieces. The translation of this geometry to a MEMS fabrication-feasible design requires the imposition of a large number of additional constraints, which would profoundly alter the device. These fabrication-oriented constraints will have as much influence on the final design as the magnetic-design issues discussed in Part I.

The primary fabrication constraints are 1) the two-dimensional (2-D) nature of micromachining, 2) a limited set of available approaches to deposit very thick structures (on the order of tens to hundreds of micrometers), and 3) fabrication-feasible methods to deposit and tightly juxtapose films of magnetic, conducting, and insulating natures.

The first fabrication constraint dictates minimization of the number of turns of conducting material in the stator design. From a micromachining point of view, each additional turn requires a multilayer process that 'stacks' conductors into a single magnetic slot. This is compounded by the need to place multiple phases within the same slot. The simplest approach is to use a single-turn, two-phase machine, which places two turns within a single slot.

One consequence of this design choice is that large currents will need to flow through the single-winding coils in order to achieve the required number of ampere-turns for successful device operation. These large currents will also result in large ohmic losses, which in turn can cause undesirable Joule heating of the machine. In addition to these coil losses, losses from the magnetic portions of the machine (i.e., eddy-current and hysteresis losses) must be considered. To quantify these effects, a set of electrothermal models must be developed to predict the temperature rise of the machine during operation.

In addition to the geometric issues discussed above, fabrication constraints also manifest themselves in terms of available materials and deposition methods for both rotor and stator. The fabrication approach adopted is based on micromolding and electroplating, which are now standard fabrication sequences for ultraminiaturized electromagnets [8]–[12]. However, with the exception of hybrid systems relying on miniaturized versions of macroscopic inductor coils [13], most successful MEMS magnetic components reported are low profile with a total thickness that does not exceed a few tens of micrometers

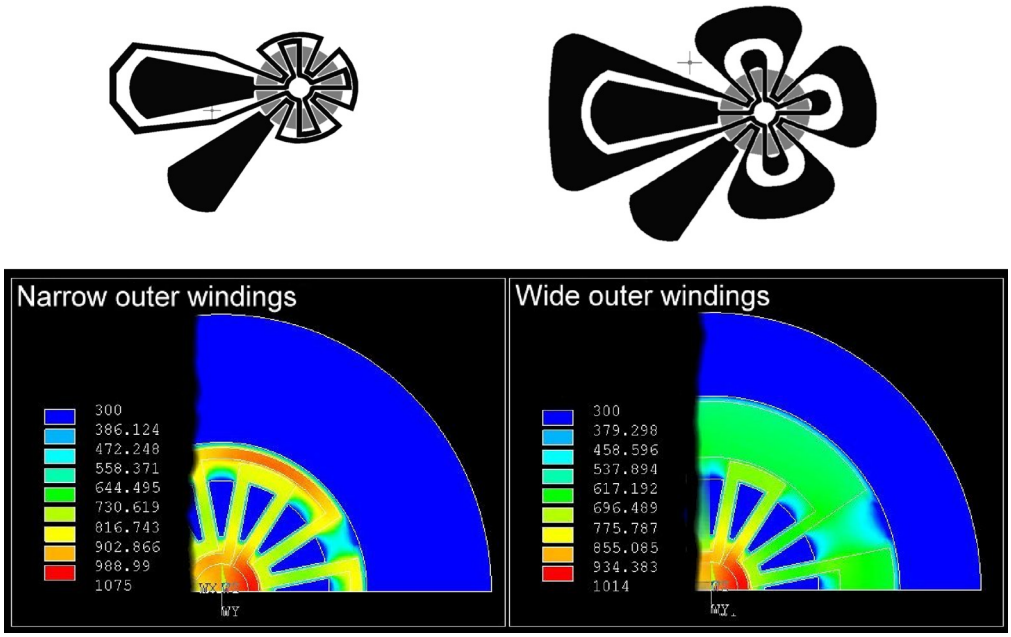

Fig. 4. Increasing outer winding width reduces the thermal stress on the stator by draining heat away from the center of the structure. Inner stator poles remain cool due to effective thermal contact with the substrate and relative thermal insulation from the windings. Temperatures are in Kelvin. (Color version available online at http://ieeexplore.ieee.org.)

[11], [14]. Since the magnetic induction machine must operate at high currents through two phases, the fabrication approach must yield multilayer structures substantially thicker (several hundreds of micrometers) than most previously reported MEMS devices.

One key element in the creation of ultra-thick multilayer micromolds is the use of thick polymers that can be patterned using conventional UV photolithography. In this work, we employed two negative photoresists: NR9-8000-P Futurrex negative photoresist (PR) and SU-8 photosensitive epoxy. The PR is used as the electroplating mold and is later removed once the plating sequence ends. The epoxy SU-8 is employed as a permanent mold that remains embedded in the stator and insures the structural integrity of the final device. The excellent planarizing properties of SU-8 allow successful patterning of such a thick layer using conventional contact photolithography, regardless of the pre-existing topography of the substrate. As Fig. 1 shows, the presence of an underlying high-aspect ratio structure does not affect the quality and resolution of a subsequent photolithographic step involving SU-8. Note that the combination of these two materials allows the elimination of a time-consuming anisotropic etch step through these multi-hundred microns-thick materials.

Electrodeposition is utilized for both the conductor and magnetic-core materials. Copper is an excellent choice for the coils due to its low resistivity and the fact that it has been demonstrated to form thick ($>$100 micrometers), low-stress microstructures. Copper structures are electroplated using $CuSO_4$-H_2SO_4-H_2O_2 electroplating bath, as described in [11].

The magnetic core material is a more difficult choice to make. Using a single material for the magnetic flux path of an electromagnetic device requires a compromise in material properties and performance. High torque output from the induction motor requires a magnetic material with large saturation flux density ($B_{\rm sat}$); however, minimizing eddy-current losses dictates a highly resistive core material. Power output from the magnetic induction machine increases with operating speed and frequency; nevertheless, the higher the frequency, the larger the eddy-current and hysteresis losses. Thus, sustaining a large torque at high frequencies requires a material with a high electrical resistivity, a high $B_{\rm sat}$ and a small coercivity value. Although it does not satisfy all of these constraints, the chosen magnetic material is permalloy Ni-Fe (80%-20%), which can be easily electrodeposited in thick ($>$100 micrometers), low-residual-stress films. The magnetic saturation flux density of the electroplated Ni-Fe is close to 0.9 T and its relative permeability is approximately 3000 before saturation. Ni-Fe 80-20 has an electrical resistivity of 5.5×10^{-7} Ω·m at room temperature. The detail of the electroplating setup and bath composition can be found in [11].

A solid model of a micromachining-compatible magnetic induction machine, which satisfies the magnetic-design constraints of Part I as well as the fabrication-design constraints discussed above, is shown in Fig. 2. The machine consists of a stator fabricated on a magnetic substrate, and a rotor suspended over the stator. An axial air gap is present between the rotor and stator. The pattern of stator windings is dictated in part by the fabrication constraints and in part by electrothermal modeling (discussed below).

The device operates in standard induction-machine fashion. The rotor is a solid magnetic disk that supports a highly conducting layer at the air gap. The stator consists of two phases of a single winding each, with either six or eight pole pairs. With its coils excited in temporal quadrature, the stator supports a traveling magnetic field wave on its surface. This field in turn induces currents in the rotor conductor with which it interacts to

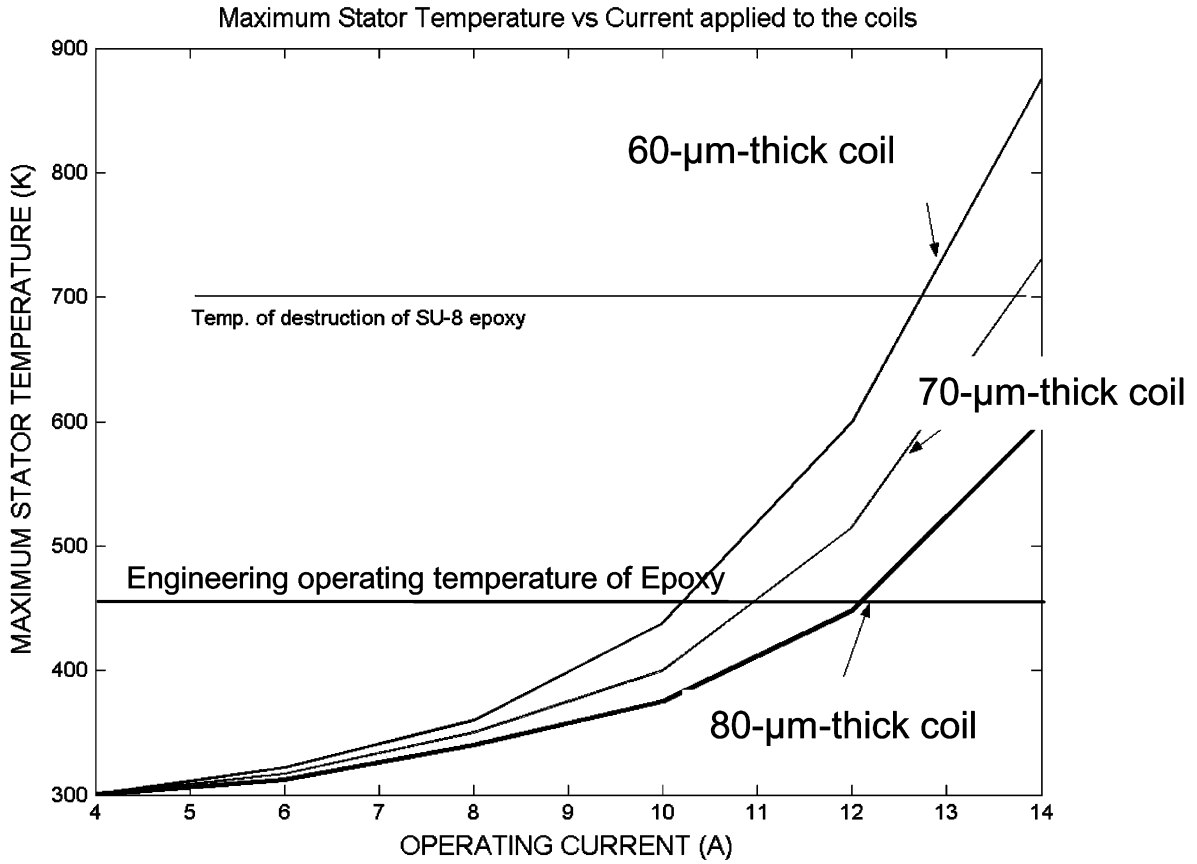

Fig. 5. Maximum temperature at the center of the stator. Depicted around 700 K is the destruction temperature of SU-8 epoxy, the structuring polymer used in stator fabrication. The glass transition temperature of SU-8 is around 473 K.

produce a torque on the rotor. Such operation can lead to both motoring and power generation.

Although the geometric parameters of the stator have been determined, the overall thickness of the windings (and therefore of the total device) is strongly influenced by electrothermal constraints. Because the machine is a low-voltage, high-current induction machine, significant amounts of current flow in the coils [15], [16]. Large ac currents mean considerable heat dissipation inside the coils, as well as potentially significant losses within the ferromagnetic core due to eddy-currents and hysteresis. The energy dissipated through hysteresis inside the ferromagnetic core is proportional to the total volume of ferromagnetic material, the operating frequency, and the total energy lost during one hysteresis cycle of the ferromagnetic material. The ferromagnetic material used for this application is electroplated Ni-Fe (80%-20%), whose low frequency magnetic properties [17], [18] are used to estimate the hysteresis loss. The two other dissipative phenomena are estimated through a 2-D finite-element magnetic analysis at various operating frequencies, keeping the excitation current density (1.9×10^9 A/m^2) constant for a 20-μm-thick, 200-μm-wide coil geometry.

Fig. 3 shows the three loss mechanisms evident in the stator under typical operating conditions. Coil and eddy-current losses were calculated using ANSYS while hysteresis losses were calculated by considering the B-H curve of the magnetic material assuming saturated conditions (a worst-case scenario). For

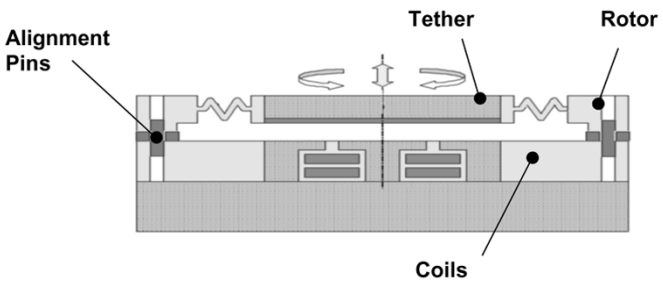

Fig. 6. In a tethered motor, the rotor is supported by tethers above the stator. These tethers are extremely stiff in the out-of-plane direction, and relatively compliant in the axial direction.

suboptimal coil geometry, heat dissipation inside the stator is dominated by winding losses. These losses will dictate that 'hot spots' may occur in the coils. As the coils are both electrically and thermally insulated from one another—as well as from the Ni-Fe slots—by a polymer, the coil-to-substrate thermal conduction path is impeded. On the contrary, heat generated in the Ni-Fe stator core can be efficiently drained via a heat sink at the bottom of the substrate; this is because the stator core is not thermally insulated from the Ni-Fe substrate wafer. It is vital to carefully optimize the coil geometry while respecting design rules and limitations arising from the fabrication approach and from the electromagnetic design. Therefore, our subsequent thermal-design efforts concentrate on refining the coil geometry to minimize winding losses and temperature rise.

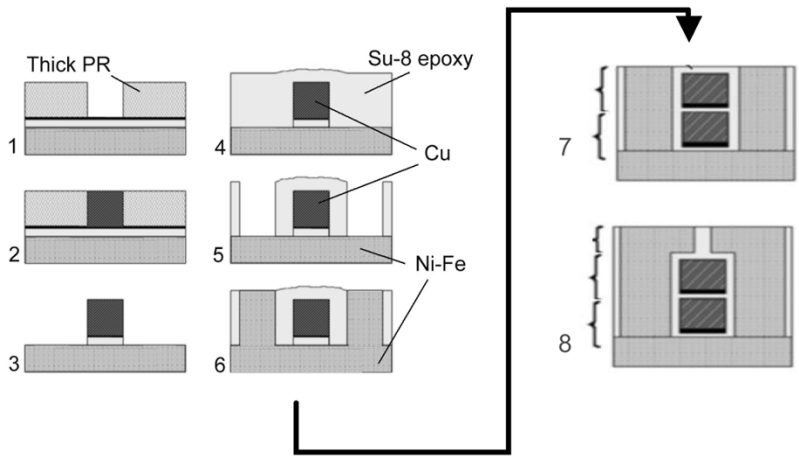

Fig. 7. Fabrication sequences to create the first metal layer (winding and core) of the stator (1 through 6) are repeated to obtain the second metal layer (7). A final Ni-Fe electroplating step followed by lapping and polishing completes the stator (8).

Optimizing the coil geometry requires that the coil cross section be maximized. One straightforward approach is to decrease the coil resistance by optimizing the in-plane turn width. Given the eventual application and the need to potentially accommodate bearings in the center of the device [1], real-estate is more readily available along the outer end-turns of the coil. Fig. 4 depicts the results of a two-dimensional ANSYS analysis, neglecting vertical conduction and convection, which is used as a simplified design tool to compare relative outer-coil geometries (this 2-D analysis will not result in accurate prediction of the central temperature). The resultant temperature map inside the stator for two different coil geometries is shown. In both cases, the coil thickness is kept at 20-μm and the current density is constant at 3×10^8 A/m^2. Fig. 4(left) displays the temperature distribution inside a single winding whose width is kept constant as it meanders around the Ni-Fe slots. Excessive heating is encountered around the outer end-turns. In Fig. 4(right), widening the outer-coil windings eliminates excessive heating at the periphery of the stator. Further increase of the width of the outer windings offers limited benefits.

To include both the influence of heat conduction through various layers of the stator, as well as the convective effects at the upper surface (thereby allowing accurate calculation of the center and inner end-turn device temperatures), a full three-dimensional (3-D) thermal model of a portion of the device is developed. Here, copper is the coil material and SU-8 epoxy is used both as an insulator and a structuring material. Simulation results indicate that it is imperative for the bottom side of the stator to be efficiently heat-sunk.

Fig. 5 shows the results of the full 3-D thermal model, giving the maximum temperature reached inside the stator as a function of coil current, as parameterized by three coil thicknesses (60, 70, and 80 μm). The horizontal line in Fig. 5 indicates the temperature at which cured SU-8 epoxy starts to decompose (700 K), and represents a hard limit of temperature. Since some papers have reported softening of SU-8 at 200 °C [21], this temperature will be considered as an "engineering limit" for the stators. Beyond this lower limit, the structural integrity of the device may be compromised. It can be seen from Fig. 5 that the coil thickness should be larger than 80 μm to safely conduct currents as high as 12 A (rms). The equivalent current density is 7.5×10^8 A/m^2, which is significantly larger than what macroscale machines can typically accommodate[1] (10^7 A/m^2). Current densities in carefully designed micromachines can reach such high values because the ratio of cooling surface area to heating volume increases inversely with the typical dimension; as a result, in the MEMS scale, cooling is much more effective. Tests conducted later on with electroplated copper microstrips embedded in a matrix of SU-8 and surrounded by Ni-Fe structure repeatedly supported dc current densities in excess of 5×10^8 A/m^2 before thermal failure. Better heat sinking techniques could potentially improve this number further.

III. Tethered-Motor Fabrication

Exploring and characterizing the operating behavior of the magnetic-induction micromachine as a generator requires that the machine operates in the presence of a power-MEMS-based mechanical work generator, such as silicon-based turbomachinery [1]. The design and fabrication alone of a rotor able to rotate at such operating speeds (around 2.4×10^6 rpm) raises design and fabrication issues for the air and thrust bearing system. It also raises integration issues as the rotor and the stator are composite microstructures that include materials other than silicon. At this stage, we adopt a design-and-testing strategy that was previously demonstrated during the development of an electrostatic induction machine [3], [4], and that is independent from the silicon-based gas turbine. The magnetic machine can be operated as an actuator in which the rotor is tethered to a series of flexible structures (see Fig. 6). In this fashion, the machine is not operated as a motor per se, since the tethers prevent the rotor from making a complete revolution. Instead, the tethers serve as a mechanical transducer of torque to deflection. More importantly, even though the rotor does

[1]It is interesting to note here that the pure AC nature of the current excitation and the relatively wide cross-sectional dimensions of the copper coils (compared to the typical grain size) yields electromigration concerns negligible throughout the duration of these experiments [19]. In fact, no discernable change in the room temperature resistance of the coils was observed during testing.

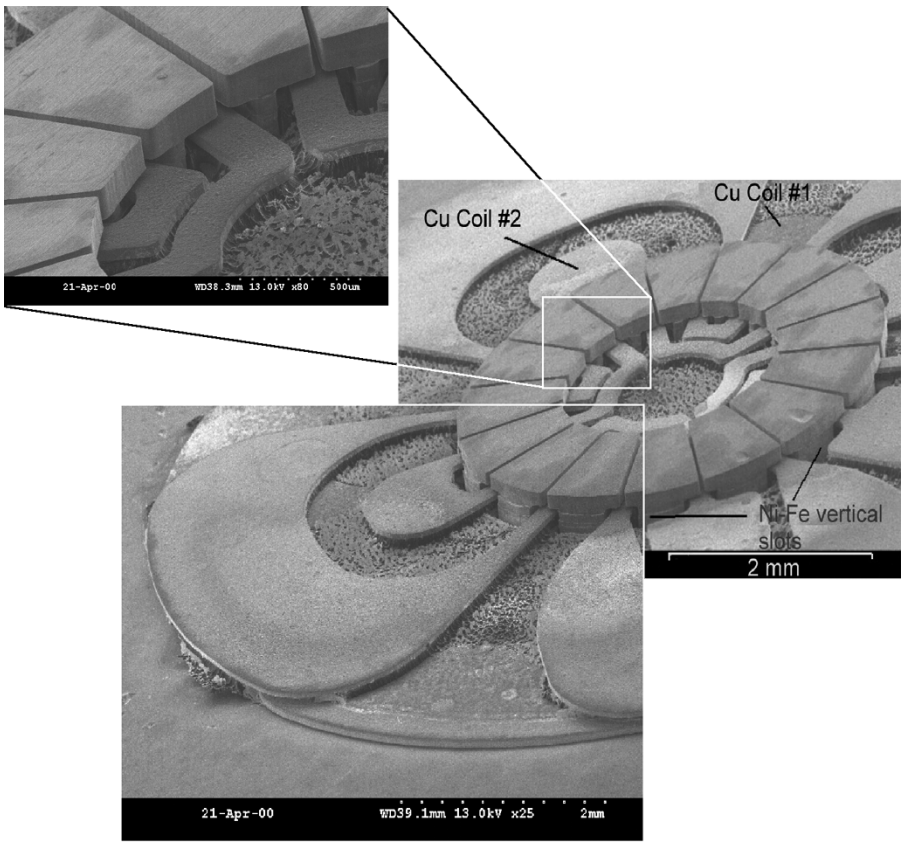

Fig. 8. SEM photograph of a functional two-coil stator with a solid Ni-Fe core.

not make a complete revolution, the motoring performance (torque) of the machine can be deduced from the deflection of the tethers. Carefully designed and fabricated supporting flexural beams can maintain the rotor at an effectively constant distance above the stator while allowing a small range of in-plane displacements. As the two phases of the stator are actuated, the rotor experiences an axial (in-plane) torque. By periodically reversing the applied torque, the mechanical resonance of the rotor and tethers can be excited and monitored for a wide range of reversal frequencies via an *in situ* motion-analysis system [20]. The angular deflections of the tethered rotor as a function of this reversal frequency can be used to determine the rotor torque. Torque measurements taken in this fashion are quite accurate, as potential obscuring effects of the air-bearing dynamics are eliminated.

A. Stator Fabrication

Fabrication steps for the stator involve three electroplated metal layers over a 1-mm-thick Ni-Fe wafer. An insulation layer of SU-8 epoxy (25 μm) is spun, cross-linked and cured. A thin Ti/Cu/Ti (30 nm, 200 nm, 30 nm) layer is deposited by dc sputtering. A 100-μm-thick NR 9-8000-p layer is then spun and processed to obtain a mold for the first copper coil [see Fig. 7(1)]. Once 80 μm of copper is electroplated, the mold is dissolved in acetone, the seed layer is selectively etched using a 2% solution of HF:H2O for the Ti layers and a solution of $CuSO_4$:NH_4OH for the layer of Cu. The insulating epoxy is removed via a quick nondirectional plasma etch [see Fig. 7(2, 3)]. A thick layer of epoxy is then spun on top of the first copper structure [see Fig. 7(4)]. The epoxy permits excellent step coverage of the surface above the pre-existing copper structures. The top SU-8 layer is later patterned by conventional photolithography in order to create a mold for the Ni-Fe slots [see Fig. 7(5)]. At this point, the copper coil is completely embedded in the epoxy. Ni-Fe is electroplated directly on the Ni-Fe substrate inside the cavities formed in the SU-8 layer [see Fig. 7(6)]. The upper surface is lapped and polished to complete the first level of the coil and the Ni-Fe core. A similar sequence is repeated in order to stack a second metal layer (coil and Ni-Fe vertical slots). A final micromolding and Ni-Fe electrodeposition, followed by a lapping and polishing sequence, completes the stator fabrication.

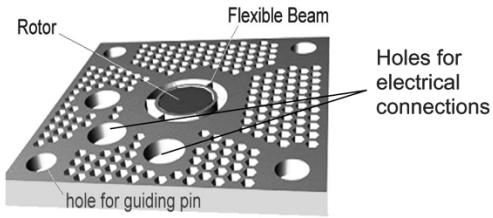

Fig. 9. A 3-D rendering of a tethered rotor die. This ultrathick die was fabricated out of released SU-8 with a 500-μm-thick Ni-Fe core, bearing an 8-μm aluminum layer on the bottom, facing the stator.

Fig. 8 shows three SEM photographs of the completed stator. Here, the epoxy has been partially removed so that the electroplated copper structures may be clearly observed. The total height of the device, excluding the substrate, is close to 500 μm.

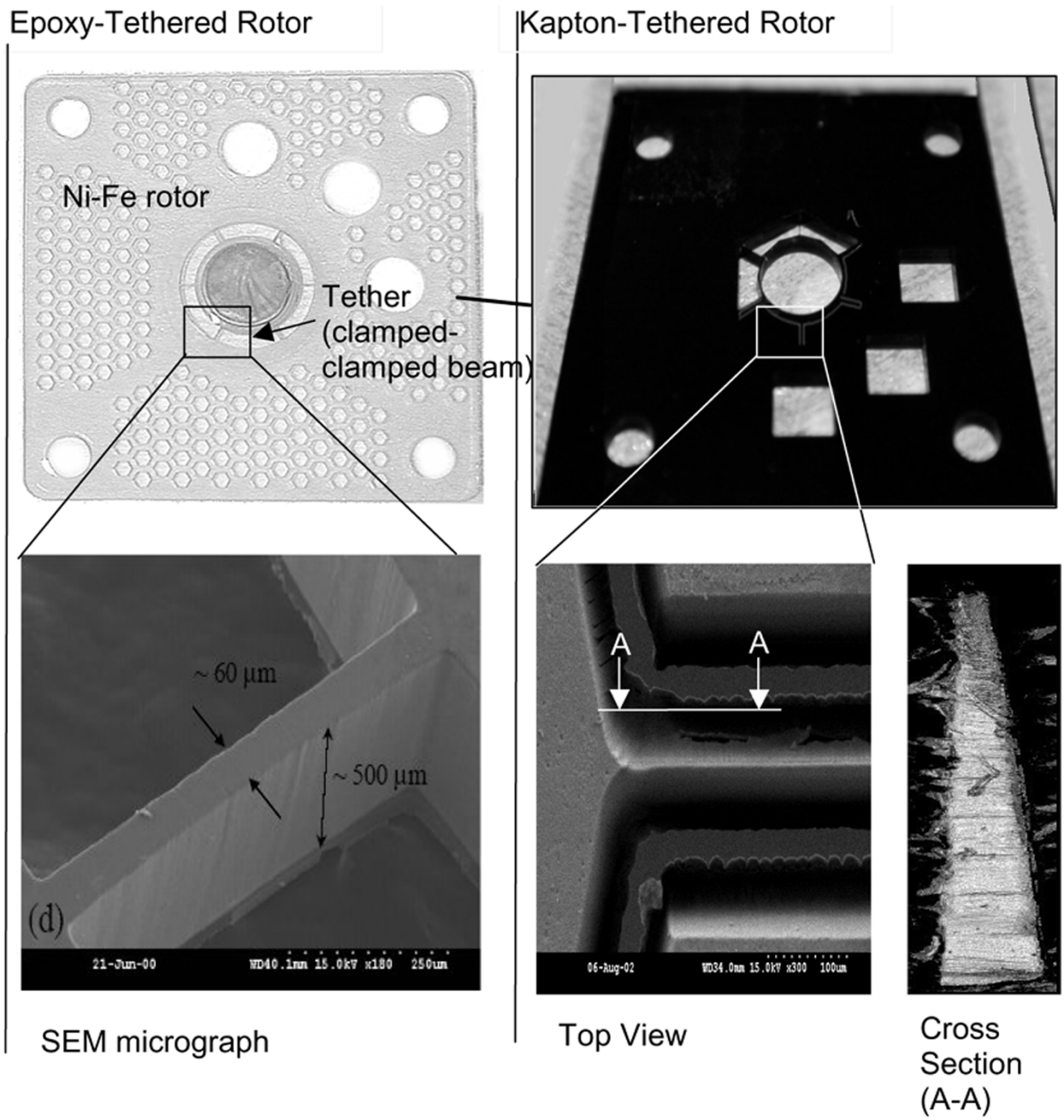

Fig. 10. SEM photograph of SU-8 (left) and Kapton tethers (right). The SU-8 tethers have a well-defined rectangular cross section whereas Kapton tethers are tapered.

B. Rotor Fabrication

To characterize the operation of the magnetic-induction machine, we designed and fabricated a tethered rotor for the induction machine. As discussed above, the tethers are flexible in the plane of the rotor allowing the rotor to partially rotate. Fig. 9 presents a rendered view of a tethered rotor die, which is a composite structure: a Ni-Fe disk 4 mm in diameter and 500 μm thick, assembled inside a mechanical system of flexible beams. The tethers hold the rotor core in place and provide a restoring force when torque is applied to the rotor. The number of tethers (six in this case) was chosen to minimize out-of-plane deflections, while maintaining relative compliance for in-plane rotations.

The rotor die was fabricated from either cross-linked SU-8 epoxy or thick, laser-etched Kapton film. Both Kapton and epoxy exhibit a low Young's modulus. Since neither material is brittle, tethers fabricated with such materials are more robust than micromachined silicon beams [3]. Dimensions for both SU-8 and Kapton tethers were chosen to result in deflection amplitudes well below the width of the tether beams, thereby keeping the deflection dynamics linear. As long as the deflection dynamics were kept linear, torque measurements could be made using the entire resonance curve of the rotor (as shown in the next section), without the need to determine the spring constant of the tethers.

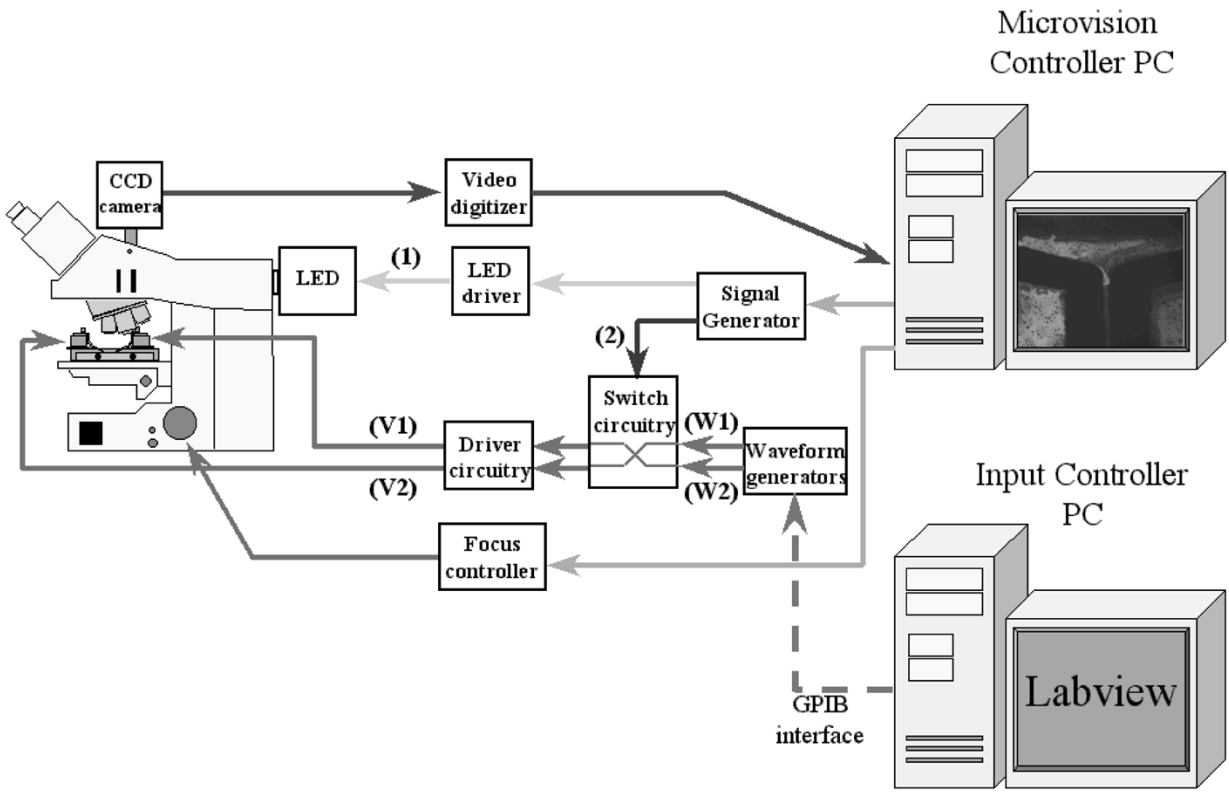

Fig. 11. Block diagram of the complete test setup.

SU-8 tethers were fabricated by spinning and processing a 500-μm-thick layer of epoxy. After photolithography and development, the structure was delaminated from the substrate through the removal of a sacrificial layer, such as aluminum. As the fabrication relied entirely on a single photolithography step, the geometrical attributes of the structures were defined with high accuracy and controllability. Fig. 10(left) shows a SEM photograph of a SU-8 tether. In general, this simple fabrication approach yields suitable tethered rotors that can be utilized as long as the temperature of the tethered structure does not exceed the engineering temperature limit of the epoxy (about 200 °C). The fabrication of Kapton tethers was comparatively more complex. The tethers were bulk micromachined from a 500-μm-thick Kapton foil using a computer-controlled Excimer laser ablation system operating at 248 nm. It was observed that the laser machining process creates Kapton beams with a significant thickness taper [see Fig. 10(right)]. In order to obtain a linear spring behavior, care was taken to ensure that the expected maximum deflection amplitude would be much smaller than the thickness at the thin end of the tethers.

The Ni-Fe rotor cores were fabricated separately. Using conventional electroplating and micromolding techniques, Ni-Fe disks 500 μm thick and 4 mm in diameter were fabricated inside molds defined in a thick layer of SU-8. The disks were later removed from their mold and their bottom (flatter) side was coated with an approximately 8-μm-thick layer of aluminum using physical vapor deposition. The rotor mass and geometry were recorded. The rotors were hand assembled and glued inside the central ring of either the SU-8 or the Kapton tether die. The tethered rotor was placed on top of the stator and aligned via four guiding pins near the corners of the die. The rotor-stator gap was controlled using thin, laser-machined Kapton shim layers of various thicknesses.

IV. Testing and Analysis of the Tethered Motor

In order to test the device, the coils of the two stator phases are connected to a high-current push-pull amplifier driven by external, phase-controllable electronics, and excited by a sinusoidal current at a frequency of f_e. As the two phases of the stator are excited in temporal quadrature, the stator supports a traveling magnetic field wave on its surface, which in turn induces currents in the rotor conductor with which it interacts to produce torque. The rotor experiences both a pull-in force (resisted by the tethers) and an axial torque (permitted by the tethers). The torque produced by the motor is directly measurable through the bending of its tethers, and is un-obscured by bearing behavior. Since the details of the mechanics of the tethers are not known, a resonance technique is used to determine the torque. A torque reversal switch in the external electronics swaps the phase excitations in the stator, changing the direction of the applied torque at reversal-frequencies f_r far lower than the input electrical excitation frequency f_e. By periodically reversing the torque, the fundamental axial mechanical resonance of the tethered rotor is excited.

The magnitudes of both the in-plane and out-of-plane rotor deflections are monitored for a wide range of reversal frequency values using a computer Microvision System [20]. Fig. 11 presents a block diagram of the test setup, and Fig. 12 depicts the timing of the relevant signals in the circuitry. Fig. 13

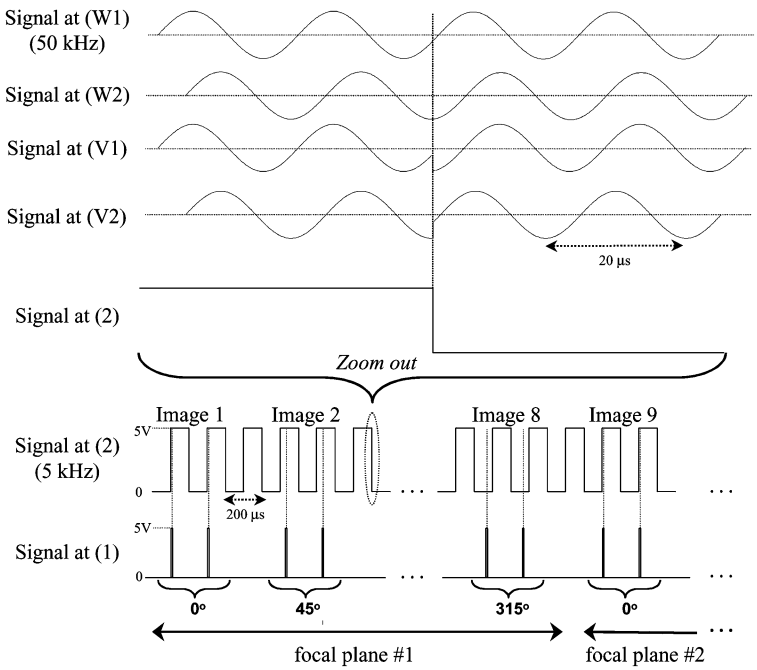

Fig. 12. The timing of some of the relevant signals from Fig. 12. The torque reversal signal switches the connections between the two phases, thereby reversing the torque on the rotor. Multiple exposure images at various delays (with respect to the onset of the torque reversal signal) and different focal planes are used by a computer microvision system to reconstruct the fundamental of the 3-D periodic displacement of the rotor.

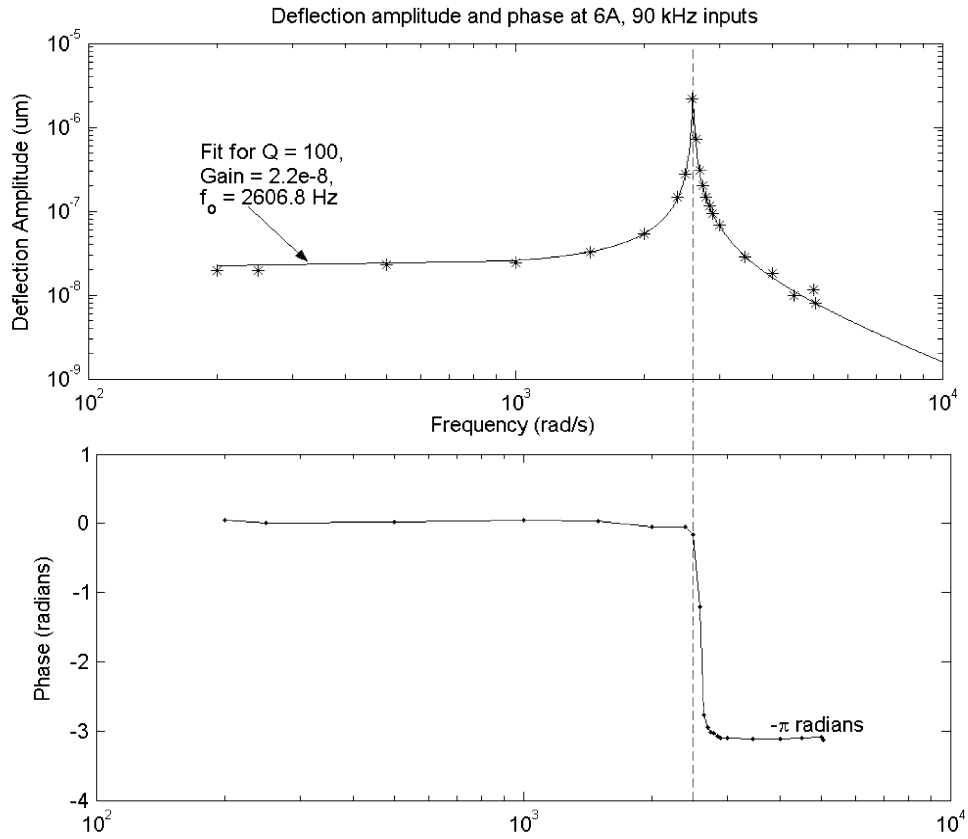

Fig. 13. Measured mechanical resonance curve set (fundamental deflection amplitude and phase) and the associated fit used to extract torque. Deflection data are taken at the base of the tethers, 2.1 mm from the rotor's center.

illustrates a sample measurement of the azimuthal tether deflection as a function of the reversal frequency, as measured using the Microvision System.

The resonance plot of Fig. 13 can be used to determine the torque produced by the motor without the need to independently ascertain the mechanical properties of the tethers. Assuming

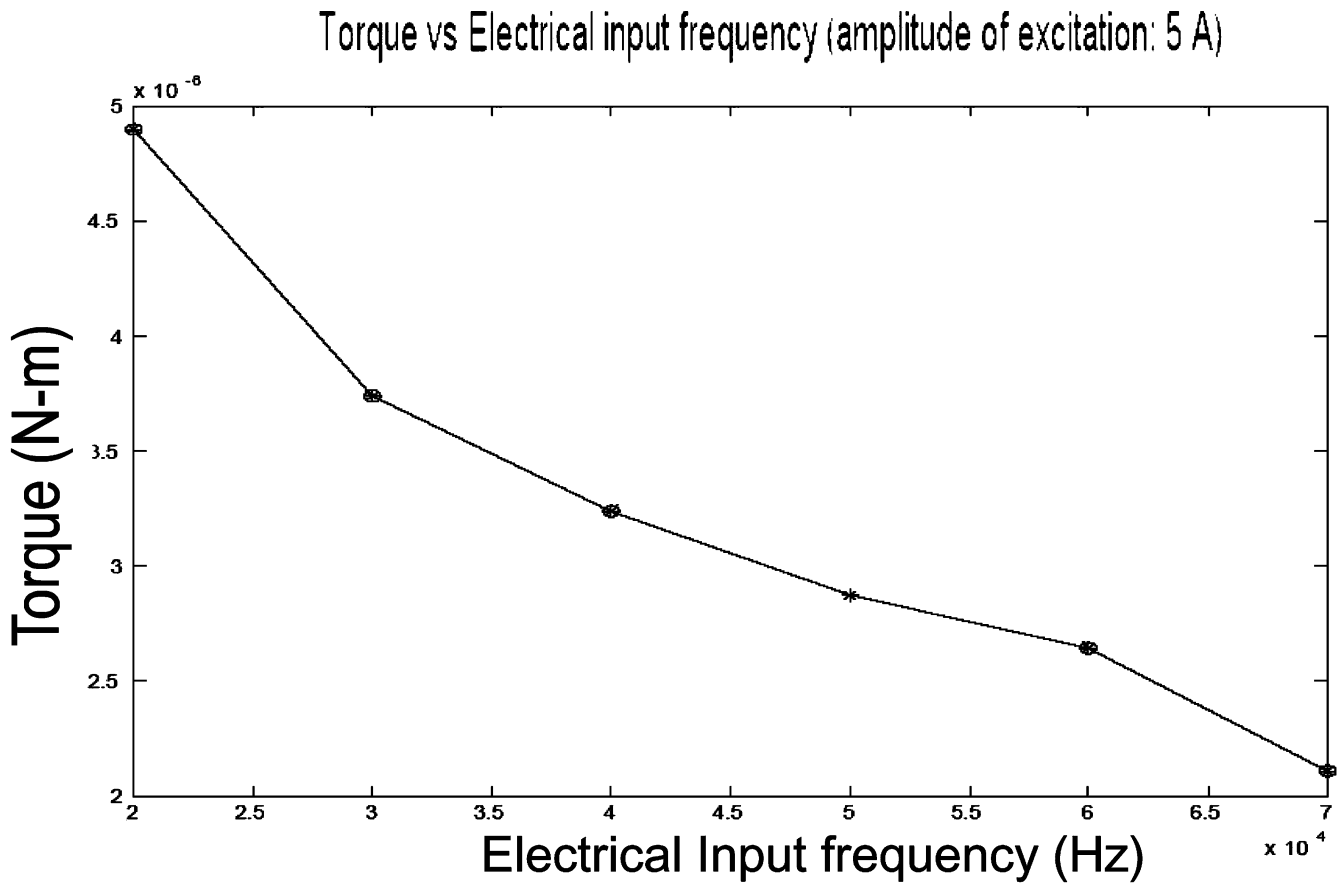

Fig. 14. Measured torque values from a SU-8 tethered structure for various excitation frequencies.

linearity and small deflections of the tethers, the mechanical dynamics of the rotor-tether structure can be described with a simple, second-order linear ordinary differential equation:

$$J\ddot{\theta} + b\dot{\theta} + k\theta = \tau(t). \tag{1}$$

Here, $\theta(t)$ is the angle of axial rotation at the measurement radius r_m that corresponds to the outer diameter of the supporting ring that encloses the rotor. Hence, $\theta(t)$ is given by $x(t)/r_m$, where $x(t)$ it the tangential deflection at the measurement radius extracted by the Microvision System. The inertial moment is given by $J = 1/2M_r \times r^2$ where M_r is the mass of the rotor plus the surrounding enclosure ring of the rotor die. The contribution to the inertial moment from the relatively small mass of the tethers themselves is neglected. Finally, k is the spring constant of the six tethers and b is the damping coefficient.

As the electrical excitation in the stator is periodically switched, the torque is expected to be a square wave that can be expressed in its Fourier components:

$$\tau(t) = \sum_{n=1,n=\text{odd}}^{\infty} \tau_0(f_e, I) \times \text{Im}\left(\frac{4}{n\pi} e^{jn\omega t}\right). \tag{2}$$

The linearity of (1) implies that the measured angle deflection is given by:

$$\theta(t) = \sum_{n=1,n=\text{odd}}^{\infty} \text{Im}(\Theta_n e^{jn\omega t}). \tag{3}$$

Substituting (2) and (3) into (1), matching terms for every Fourier mode, solving for Θ_n, and using $|X_n| = r_m|\Theta_n|$, we can express the amplitude of the tangential displacement X_n as

$$|X_n| = \frac{G\omega_0^2 \frac{4}{\pi n}}{\sqrt{\left(\omega_0^2 - n^2\omega^2\right)^2 + \left(\frac{n\omega\omega_0}{Q}\right)^2}} \tag{4}$$

where $\omega_0 = \sqrt{k/J}, Q$ is the quality factor defined as $Q = \sqrt{J\omega_0/b}$, and G is the gain factor given by $G = \tau_o(f_e, I)(r_m)/(J\omega_0^2)$. The phase of the deflection is given by

$$\angle X_n = -\arctan\left(\frac{\omega_0 n\omega/Q}{\omega_0^2 - n^2\omega^2}\right). \tag{5}$$

Finally, the overall deflection is the sum of all Fourier components

$$X(t) = \sum_{n=1,n=\text{odd}}^{\infty} |X_n| \sin(n\omega t + \angle X_n). \tag{6}$$

Equations (4) and (5) are expressed in terms of the natural frequency and the quality factor of the mechanical system, both of which are rather easy to extract from a given resonance curve. The Microvision System gives a direct measurement of the fundamental $(n = 1)$ for the deflection amplitude and phase in (4) and (5). G, Q as well as ω_0 are fitted to the resonance curves. The applied torque is extracted by making a-second order system fit to the fundamental terms of (4) and (5) with

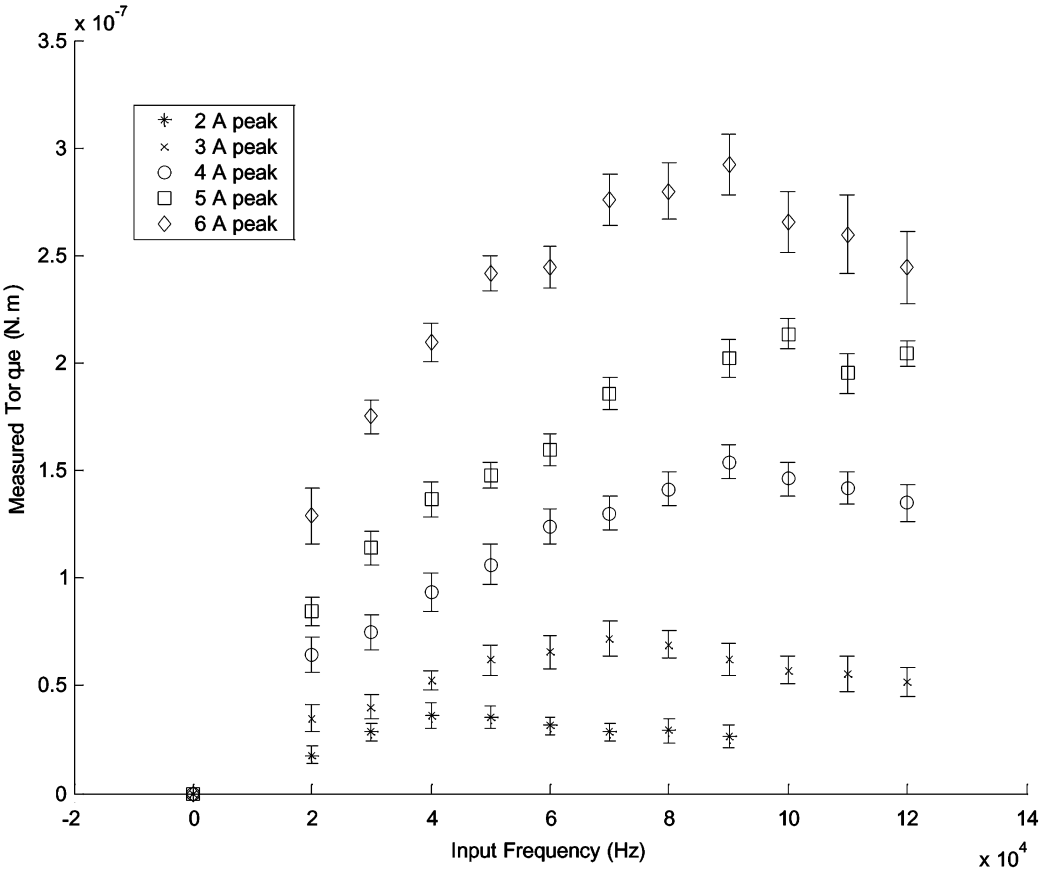

Fig. 15. Systematic torque measurements from a Kapton tethered micromotor.

G, ω_0, and Q as parameters. Our system has a relatively high Q factor (around 100), which makes it easy to determine the natural frequency of the tether-rotor system. The only critical fit parameter for accurate torque determination is the gain factor, G. Hence, the measurement of the torque does not require knowing the tether dimensions and mechanical properties of the constituting material, which greatly simplifies the analysis.

Using the approach outlined above, experiments with SU-8 tethers were conducted for various excitation currents (2 to 5 A) and excitation frequencies (20 to 70 kHz); the corresponding torque was extracted each time. The first set of experiments using SU-8 tethers revealed that micromotor heating at high currents raised the temperature of the device up to and beyond the engineering temperature limit of the SU-8 (approximately 200 °C once cross-linked). The accompanying deterioration in the mechanical properties of the SU-8 caused the tethers to warp in both the azimuthal and the axial directions. As a result, the air gap was reduced substantially, presumably due to the inability of the SU-8 to withstand the pull-in forces under this high temperature condition. However, if such devices were still functional, they possessed extremely small air gaps and therefore high forces. For example, in one of the devices with nonzero air gap, the torque results of Fig. 14 were obtained. The amplitude of the stator currents was approximately 5 A. It is estimated that the air gap corresponding to the data was approximately 5 μm.

The maximum torque extracted from the SU-8 tether device was 4.8 μN-m for an excitation frequency of 20 kHz. It is likely that the air gap was changing as the input frequency was varied. Hence, Fig. 14 does not provide a reliable source of data against which the electromagnetic model can be tested. Using higher temperature Kapton tethers, more reliable and systematic data with a controlled air gap were obtained; albeit at lower achieved torques. The data obtained, presented in Fig. 15, proved repeatable and much more amenable to magnetic analysis.

The results obtained with the Kapton tethers are one order of magnitude lower than the results obtained using epoxy tethers, peaking at approximately 3×10^{-7} N-m for a excitation current amplitude of 6 A at 90 kHz. This reduction in torque is partly due to a larger air gap. Since Kapton is less sensitive to temperature changes (up to 350 °C), the air gap was maintained at its initial value set by the spacing layer and the structure of the rotor (70 μm overall). As the torque is inversely proportional to the air gap, a larger air gap translates into a reduction of the torque experienced by the rotor above the stator. Experiments involving Kapton tethers and gaps smaller than 70 μm were not performed.

V. Conclusion

The geometric optimization (subject to fabrication, thermal, and magnetic constraints), fabrication, and testing of a mi-

croscale magnetic induction two-phase tethered planar motor has been demonstrated. The machine is, by electromagnetic design, a low-voltage, high-current induction machine. The fabrication approach is based on micromolding and electroplating optimized for ultrathick multilayered magnetic microsystems able to handle very high operating currents. Thermal optimization of the stator has revealed a need to widen the winding end-turns to reduce thermal stresses on the structure. To characterize the operation of the magnetic induction micro machine, tethered motors were designed and fabricated in order to accurately determine the output machine torque. The stators and tethered rotors were built separately and hand-assembled prior to testing. The maximum torque from a device with SU-8 epoxy rotor tethers was determined to be of 4.8 μN-m when driven at $5\mathrm{A}$ and 20 kHz. However, it was observed that temperature elevation in the stator caused the SU-8 tethers to warp, reducing the air gap and correspondingly increasing the torque significantly. Experiments based on Kapton tethers and a much larger air gap resulted in more systematic and reliable torque data, with a maximum of around 0.3 μN-m at a stator current of $6\mathrm{A}$ and excitation frequency of 90 kHz. Next generation of stators may benefit from refining the fabrication technology further, such as by creating wider outer-turns. Such geometrical changes retain the potential to further minimize the impact of hot-spots, potentially detrimental for long term operation and would allow the machine to operate at higher current levels.

ACKNOWLEDGMENT

The authors would like to thank S. D. Senturia for helpful discussions.

REFERENCES

[1] A. H. Epstein *et al.*, "Power MEMS and microengines," in *Proc. IEEE Int. Conf. Solid State Sens. Actuators*, vol. 2, Chicago, IL, Jun. 1997, pp. 753–756.

[2] K. Fu, A. J. Knobloch, F. C. Martinez, D. C. Walther, A. P. Pisano, and D. Leipmann, "Design and fabrication of a silicon-based MEMS rotary engine," in *Proc. MEMS, 2001 ASME Int. Mech. Eng. Congr. Exp.*, 2001, pp. 875–880.

[3] S. F. Nagle, "Analysis, Design and Fabrication of an Electric Induction Micromotor for a Microgas Turbine Generator," Ph.D. dissertation, Massachusetts Institute of Technology, Cambridge, MA, Oct. 2000.

[4] H. Koser, "Development of Magnetic Induction Machines for Micro Turbo Machinery," Ph.D. dissertation, Massachusetts Institute of Technology, Cambridge, MA, Jun. 2002.

[5] J. Park, S. H. Han, and M. G. Allen, "Batch-fabricated microinductors with electroplated magnetically anisotropic and laminated alloy cores," *IEEE Trans. Magn.*, vol. 35, no. 5, pp. 4291–4300, 1999.

[6] J. Park, J. Y. Park, Y. Joung, and M. G. Allen, "Fabrication of high current and low profile micromachined inductor with laminated Ni/Fe core," *IEEE Trans. Compon. Packag. Technol.*, vol. 25, pp. 106–111, 2002.

[7] J. Park, F. Cros, and M. G. Allen, "A sacrificial layer approach to highly laminated magnetic cores," in *Proc. IEEE Int. Conf. MEMS*, Las Vegas, NV, Jan. 2002, pp. 380–383.

[8] M. Xu, T. M. Liakopoulos, C. H. Ahn, S. H. Han, and H. J. Kim, "A microfabricated transformer for high-frequency power or signal conversion," *IEEE Trans. Magn.*, vol. 34, pp. 1369–1371, 1998.

[9] O. V. Seidemann and S. Buttgenbach, "Microcoils and microrelays: An optimized multilayer fabrication process," *Sens. Actuators A, Phys.*, vol. 83, pp. 124–129, 2000.

[10] M. Ruan, J. Shen, and C. B. Wheeler, "Latching micro magnetic relays with multistrip permalloy cantilevers," in *Proc. IEEE Int. Conf. MEMS*, Interlaken, Switzerland, Jan. 2001, pp. 224–227.

[11] W. P. Taylor, "The Design and Fabrication of Fully Integrated Magnetically Actuated Micromachined Relays," Ph.D. dissertation, Georgia Institute of Technology, Atlanta, GA, 1998.

[12] W. P. Taylor and M. G. Allen, "Integrated magnetic microrelays: Normally open, normally closed, and multi-pole," in *Proc. IEEE Int. Conf. Solid-State Sens. Actuators*, vol. 2, Chicago, IL, Jun. 1997, pp. 1149–1152.

[13] T. R. Christenson, T. J. Garino, E. L. Venturini, and D. M. Berry, "Application of deep X-ray lithography fabricated rare earth permanent magnets to multipole magnetic microactuators," in *Proc. 10th Int. Conf. Solid State Sens. Actuators (Transducers)*, vol. 1, Jun 1999, pp. 98–101.

[14] V. Seidemann, M. Ohnmacht, and S. Buttgenbach, "An optimized multilayer fabrication process for high aspect ratio electromagnetic devices and microsystems (MEMS)," in *Proc. IEEE Int. Conf. Solid-State Sens. Actuators*, The Hague, The Netherlands, Sep. 1999, pp. 102–105.

[15] H. Koser and J. H. Lang, "Modeling a high power density MEMS magnetic induction machine," in *Proc. Int. Conf. Model. Simul. Microsyst.*, Hilton Head, SC, Mar. 2001, pp. 286–289.

[16] F. Cros, "Développement et test d'une micromachine à induction magnétique et techniques de microfabrication pour microcomposant électromagnétique," Ph.D. Thesis, Ecole doctorale de Toulouse, France, Sep. 2002.

[17] W. P. Taylor, M. Schneider, H. Baltes, and M. G. Allen, "Electroplated soft magnetic materials for microsensors and microactuators," in *Proc. IEEE Int. Conf. Solid-State Sens. Actuators*, vol. 2, Chicago, IL, Jun. 1997, pp. 1445–1448.

[18] J. W. Judy, R. S. Muller, and H. H. Zappe, "Magnetic micro actuation of polysilicon flexure structures," *J. Microelectromech. Syst.*, vol. 4, no. 4, pp. 162–169, 1995.

[19] L. M. Ting, J. S. May, W. R. Hunter, and J. W. McPherson, "AC electromigration characterization and modeling of multilayered interconnects," in *Proc. Rel. Phys. Symp.*, Atlanta, GA, Mar. 1993, pp. 311–316.

[20] W. Hemmert, M. S. Mermelstein, and D. M. Freeman, "Nanometer resolution of three-dimensional motions using video interference microscopy," in *Proc. IEEE Int. Conf. MEMS*, Orlando, FL, Jan. 1999, pp. 302–308.

[21] H. Lorenz, M. Despont, N. Fahrni, N. LaBianca, P. Renaud, and P. Vettiger, "SU-8: A low-cost negative resist for MEMS," *J. Micromech. Microeng.*, vol. 7, no. 3, pp. 121–124, 1997.

Florent Cros received the B.S. and M.S. degrees in physics and materials science from the National Institute of Applied Sciences (INSA), Toulouse, France, from 1992 to 1997. He received the Ph.D. degree in microsystems from the Ecole Doctorale de Toulouse, France, in 2002.

Later, he accepted a postdoctoral position at the Georgia Institute of Technology, Atlanta, focusing on the fabrication of a high-temperature, high-power density magnetic induction micromachine (2002–2003). Currently, he is a Research & Development Engineer at CardioMEMS, Inc., Atlanta, GA.

Hur Koser (M'03) received the B.S. degree in physics degree in 1999, and the B.S., M.Eng., and Ph.D. degrees electrical engineering and computer science from the Massachusetts Institute of Technology, Cambridge, in 1998, 1999, and 2002, respectively.

Since 2003, he has been an Assistant Professor of Electrical Engineering at Yale University, New Haven, CT. His other research interests are in the design and development of magnetic micromachines and other micropower devices, microsensors and actuators, and microfluidic devices with an emphasis on biomedical applications.

Dr. Koser has received the NSF Career Award to work on the hydrodynamics of ferrofluids in 2005.

Mark G. Allen (M'89–SM'95) received the B.A. degree in chemistry, the B.S.E. degree in chemical engineering, and the B.S.E. degree in electrical engineering from the University of Pennsylvania, Philadelphia, and the S.M. and Ph.D. degrees from the Massachusetts Institute of Technology, Cambridge, in 1989.

He joined the faculty of the Georgia Institute of Technology, Atlanta, in 1989, where he currently holds the rank of Professor and the J. M. Pettit Professorship in Microelectronics. His research interests are in the areas of micromachining and microelectromechanical systems (MEMS); in particular, the development and application of new fabrication technologies for micromachined devices and systems. He was General Co-Chair of the 1996 IEEE MEMS conference and is North American Editor of the *Journal of Micromechanics and Microengineering*.

Jeffrey H. Lang (S'78–M'79–SM'95–F'98) received the S.B., S.M., and Ph.D. degrees in electrical engineering from the Massachusetts Institute of Technology (MIT), Cambridge, in 1975, 1977, and 1980, respectively.

Currently, he is a Professor of Electrical Engineering at MIT. He has been an MIT faculty member since receiving his Ph.D. degree and his research and teaching interests focus on the analysis, design and control of electromechanical systems with an emphasis on rotating machinery, microsensors and actuators, and flexible structures. He has written over 160 papers and holds 10 patents in the areas of electromechanics, power electronics, and applied control.

Dr. Lang has been awarded four Best Paper prizes from various IEEE societies. He is a former Hertz Foundation Fellow and a former Associate Editor of *Sensors and Actuators*.